EUROnu WP2 Note 10-09

The target and horn for the SPL-based Super Beam: preliminary design report

C. Bobeth[b], O. Caretta[d], P. Cupial[a], T. Davenne[d], C. Densham[d], M. Dracos[b], M. Fitton[d], M. Kozien[a], B. Lepers[b], A. Longhin[c], P. Loveridge[d], F. Osswald[b], M. Rooney[d], B. Skoczen[a], A. Wroblewski[a], M. Zito[c]

[a]*Cracow University of Technology, Cracow, Poland*
[b]*IPHC, Université de Strasbourg, CNRS/IN2P3, F-67037 Strasbourg, France*
[c]*Irfu, CEA-Saclay, 91191 Gif-sur-Yvette, France*
[d]*STFC Rutherford Appleton Laboratory, Didcot, UK*

Abstract

The purpose of this note is to present the conceptual design of the target and horn for the SPL-based Super Beam. We first introduce the object of this study and give a rapid overview of the experimental setup. In the main part of this note we present the design of the target and horn.

Key words: Super Beam, EUROnu, neutrino oscillations, target, horn

1. The SPL based Super Beam project

The EUROnu SuperBeam work package studies the SPL (CERN) to MEMPHYS (Frjus) project, with a baseline of 130 km and a beam power of 4 MW. The Superconducting Proton Linac (SPL), is a new proton driver using superconducting radio-frequency cavities: it has been proposed to improve the performances of the CERN injector chain. SPL has been designed to satisfy the specifications for the proton driver of a neutrino factory. MEMPHYS (MEgaton Mass PHYSics) is the proposal of a megaton class water Cherenkov detector located at Frjus, at a distance of 130 km from CERN. The object of this note is a preliminary design report of the target and collector system needed for the CERN-Frjus Super Beam

November 29, 2010

experiment. This note is produced as deliverable n xx by EUROnu Work Package 2.

1.1. Overview of the CERN-Frjus Super Beam experiment

The main aim of the CERN-Frjus (C2F) Super Beam experiment is the study of neutrino oscillations beyond the current experimental effort (T2K, Double Chooz, Daya Bay, RENO). In particular, C2F is particularly suited for the measurement of CP violation as its short baseline and low energy minimizes the matter effects. CP violation will be studied running the beam for 2 years in neutrino mode and 8 years in anti-neutrino mode.

The experiment is composed of SPL, a multi MW proton driver, an accumulator ring, a target and collection system (described in detail in the following sections), a decay tunnel, a beam dump, a near detector (not covered here) and MEMPHYS, the water Cherenkov far detector.

1.2. The Superconducting Proton Linac

The CERN accelerator group, in collaboration with other European laboratories, has produced detailed studies of the Superconducting Proton Linac (SPL) [**?**], a new proton driver based on a linear accelerator and using superconducting radio-frequency cavities.

The SPL is fully compatible with the ISS reference parameters for the proton driver provided two additional rings, one for accumulation and one for compression of the pulses, are added. The design of these rings is also quite advanced [**?**]. The parameters considered for the SPL in the latest study are reported in Table 1. For high-power applications the SPL will provide a 5 GeV, multi-MegaWatt beam, whose time-structure can be tailored for each application. For a Super Beam, the bunch duration must be less than 5 μs in order to be compatible with the width of the current pulse sent to the horn. This requires only the accumulation ring whose parameters and issues will be discussed in further work by the WP2 in conjunction with the CERN accelerator group.

1.3. The beam-target interface Matt

Table 1: Parameters of the SPL [?]

Parameters	unit	SPL
Energy	[GeV]	5.0
Beam power	[MW]	4.0
Repetition rate	[Hz]	50
Average pulse current	[mA]	40
Peak pulse current	[mA]	64
Chopping ratio	[%]	62
Beam Pulse length	[ms]	0.6
Protons per pulse for PS2	[10^{14}]	1.5
Beam duty cycle	[%]	2.0
Number of klystrons (LEP)		14
Number of klystrons (704 MHz)		57
Peak RF power	[MW]	219
Average power consumption	[MW]	38.5
Cryogenics av. power consumption	[MW]	4.5
Cryogenic temperature	[K]	2.0
Length	[m]	534

2. Overview of the target and collector

In this section we briefly present the overall conceptual design of the target station and its interface with the proton driver. A schematic layout of the proton driver - target station interface is shown in Fig. 1.

The baseline design decisions are summarized as:

1. Each target is embedded within the bore of a conventional pulsed current magnetic horn inside a magnetic reflector.
2. In order to mitigate the combined technical challenges of cycling the horn at 50 Hz and of the radiation damage and heat load generated in the target material, a target station composed of 4 targets and collectors is proposed with kicker magnets used to cycle consecutive beam pulses between each target/collector.
3. A static low Z solid target material is viewed as being technically achievable.

Points 2) and 3) require further explanation. With the 4-target system, each target would accept a 1 MW beam but the heat load generated would only be

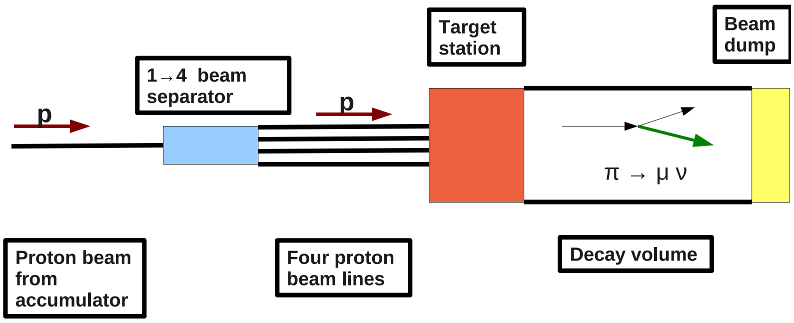

Figure 1: Schematic layout of the proton driver - target station interface.

around 50 kW for each graphite target. This is a factor of two greater than the T2K Phase 1 target and around the same as is anticipated for a T2K upgrade, and seems a reasonable objective. In addition to reducing the technical challenges, the multi-target and horn solution will increase the lifetime of both the target and horn by at least the same ratio.

From the point of view of the beam, this requires a separator to split the beam in four beam pipes. As an illustration, a kicker magnet could be used for this purpose. According to preliminary discussions with the CERN SPL experts, there does not seem to be major difficulties with this device. In term of operation, we foresee that each spill will be sent to a different target, and that therefore the operation frequency of each target and collector system will be 12.5 Hz. Finally, first studies have addressed the issue of the efficiency loss due to geometric effects in the decay volume. We have varied the radial geometrical arrangement of the four system, from close contact (each system has an overall radius of 72 cm) to the maximum distance, with the four system at the border of decay volume. The maximum loss in the neutrino beam intensity is 13 %, while the expected loss in a realistic configuration amounts only to a few percent.

A schematic layout of the target and collector system is shown in Fig. 2. The target station consists of four systems like the one shown. The parameters of the beam at the target are summarized in Table 2 while the parameters of the target and collector are reported in Table **??**.

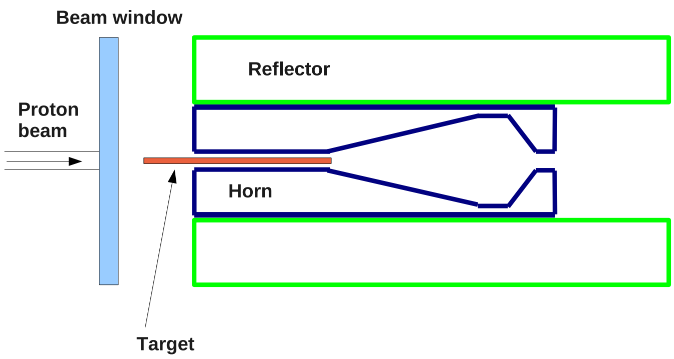

Figure 2: Schematic layout of the Super Beam target station for one of the four proton beams.

Table 2: Parameters of the SPL based Super Beam at the target.

Parameters	unit	value
Energy	[GeV]	5.0
Total Beam power	[MW]	4.0
N of beam lines		4
Repetition rate (each beam)	[Hz]	12.5
Pulse duration	[μs]	5
Beam Gaussian width	mm	4

3. The target

3.1. Conceptual design of the target Chris-Benjamin

3.2. Target: Particle production for low- and high-Z materials

The choice of the target material represents a compromise between the $\pi^{\pm}$ production rates[1] which are important for the physics application and the technical demands such as mechanical stress, cooling requirements and radiation safety issues.

In the case of solid materials the high power deposition in the target requires rather high melting points and efficient cooling in order to remove the deposited heat due to the primary beam. This problem could be avoided using liquid targets such as Hg or powder metal jets which themselves serve as heat carrier in a cooling circuit. However, the treatment of liquid Hg jets bears other difficulties such as ... The application of powder metal jets is still in the exploration phase ...

A set of mostly solid low and high atomic number (Z) materials is compared in terms of their secondary particle production and energy deposition when hit by a primary proton beam. The low-Z materials comprise Beryllium (Be), Graphite (C), Aluminium (Al) and the compound AlBeMet (mass fractions: 61 % Be, 38 % Al; 1 % O) whereas the high-Z materials are Tantalum (Ta), Tungsten (W) and the liquid metal Mercury (Hg). The secondary particle production and energy deposition is obtained with the help of simulation using FLUKA [2] with default settings for particle transport cut-off thresholds and the material properties listed in 3.

	Be	C	Al	AlBeMet	Ta	W	Hg
atomic number Z	4	6	13		73	74	80
density [g/cm^3]	1.85	1.85	2.7	2.1	16.69	19.25	13.546
melting point [K]	1560	3915	933		3290	3695	
λ_I [g/cm^2]	77.8	85.8	107.2		191.0	191.9	197.5
λ_I/ρ [cm]	42.1	46.4	39.7		11.4	10.0	14.6

Table 3: Properties of target materials.

For the purpose of comparison the target geometry is a simple cylinder of length L^{tg} and radius R^{tg} which are varied as well as the primary energy of the

[1] In the range of few GeV of primary proton energy the $K^{\pm}$ production rates are of sub-leading order compared to the $\pi^{\pm}$ ones.

proton beam $E_{\mathrm{kin}}^{\mathrm{bm}}$. The target cylinder axis coincides with the primary beam axis, which is chosen along the $+z$-direction. As a reference target tgcccmctgcccmckincbmccGeVc is taken, such that the length corresponds to roughly $2 \times \lambda_I/\rho$, i.e. twice the nuclear interaction length of the low-Z materials.

	Be	C	Al	AlBeMet	Ta	W	Hg
π^+	0.65	0.67	0.71	0.67	0.57	0.55	0.58
π^-	0.46	0.44	0.49	0.47	0.49	0.47	0.50
K^+	0.0096	0.0099	0.011	0.010	0.011	0.011	0.012
K^-	0.0003	0.0003	0.0003	0.0003	0.0002	0.0001	0.0002
K^0	0.0054	0.0055	0.0066	0.0058	0.010	0.010	0.0098
$\bar{K}^0$	0.0005	0.0005	0.0006	0.0006	0.0007	0.0008	0.0007
e^+	0.12	0.17	0.44	0.21	0.99	0.81	1.17
e^-	0.39	0.44	0.78	0.50	1.30	1.09	1.48
ν_e	0.012	0.012	0.019	0.014	0.099	0.11	0.072
$\bar{\nu}_e$	$< 10^{-4}$	$< 10^{-4}$	$< 10^{-4}$	$< 10^{-4}$	$< 10^{-4}$	$< 10^{-4}$	$< 10^{-4}$
μ^+	0.0014	0.0015	0.0018	0.0016	0.0039	0.0042	0.0034
μ^-	0.0007	0.0007	0.0008	0.0007	0.0008	0.0007	0.0008
ν_μ	0.014	0.013	0.021	0.016	0.10	0.12	0.076
$\bar{\nu}_\mu$	0.013	0.012	0.020	0.015	0.10	0.12	0.073
γ	1.87	2.22	5.70	2.80	53.8	50.2	50.9
p^+	1.47	1.60	1.90	1.62	1.60	1.47	1.80
n	2.36	1.94	3.99	2.88	43.6	47.6	41.9
Λ	0.0060	0.0062	0.0071	0.0063	0.0075	0.0074	0.0082
Σ^+	0.0007	0.0008	0.0009	0.0008	0.0007	0.0006	0.0007
Σ^-	0.0006	0.0006	0.0007	0.0006	0.0006	0.0006	0.0007
α	0.0006	0.0006	0.0006	0.0006	0.0008	0.0008	0.0011
^{3}He	0.0002	0.0003	0.0002	0.0002	$< 10^{-4}$	$< 10^{-4}$	$< 10^{-4}$
Tritium	0.0021	0.0013	0.0011	0.0019	0.0005	0.0005	0.0008
Deuterium	0.0063	0.0050	0.0044	0.0055	0.0012	0.0011	0.0015

Table 4: Total multiplicities of particles (mesons, leptons, photons, baryons and light nuclei) for different low- and high-Z target materials for the reference target.

The according secondary particle multiplicities are given in 4 for all target materials. The multiplicity is defined as the ratio of the number of secondaries when exiting the target surface and the number of primaries on target (p.o.t.). The multiplicities where obtained simulating 10^6 p.o.t. and a pencil like beam with a point-like beam spot, using a more realistic gaussian beam profile results in negligible changes. At beam energy of $E_{\rm kin}^{\rm bm} = 4.5\,{\rm GeV}$ the secondary particles are predominantly γ, n, p^+, $\pi^\pm$ and $e^\pm$, whereas other secondaries are produced with multiplicities $< 10^{-1}$, except ν_e and ν_μ, $\bar{\nu}_\mu$ for high-Z materials. Especially γ, n, p^+ and $e^\pm$ cause undesired radiation and activation, which can be reduced substantially using low-Z instead of high-Z materials. The π^+ multiplicities are around $(0.65 - 0.71)$ and $(0.55 - 0.58)$, whereas π^- multiplicities range within $(0.44-0.49)$ and $(0.47-0.50)$ for low-Z and high-Z materials, respectively. Thus low-Z materials yield about 15 % higher and about 5 % lower multiplicities for π^+ and π^-, respectively, compared to high-Z materials. The clear advantage of low-Z materials of π^+ production should be however confronted with the longer running time for π^- focusing mode for the anti-neutrino beam caused by the lower $\bar{\nu}_\mu$ and $\bar{\nu}_e$ cross sections compared to the ν_μ and ν_e ones. In principle the roughly 5 times higher multiplicities of ν_e and ν_μ, $\bar{\nu}_\mu$ for high-Z materials might lead also to higher irreducible background in the (anti-) neutrino beam. Finally, 4 shows, that there are no significant differences among the selected materials in each group of low- and high-Z materials, respectively, such that the final selection might be based on technical aspects. Strong differences appear though between both groups as explained above. Low-Z materials seem preferable concerning pion production and are clearly advantageous with respect to radiation safety due to less γ, n and $e^\pm$ production.

Figure 3: The differential multiplicity distribution of π^+ [left] and π^- [right] w.r.t. the total momentum at target exit for the reference target for low atomic number materials Be, C, Al and compound AlBeMet compared with high atomic number materials Ta, W and Hg. Numbers in brackets in the legend are the integrated multiplicities over the range shown in total momentum.

Figure 4: The differential multiplicity distribution of π^+ [upper, left] and π^- [upper, right] w.r.t. polar angle with the beam axis at target exit for the reference target for low atomic number materials Be, C, Al and compound AlBeMet compared with high atomic number materials Ta, W and Hg. [lower, left] and [lower, right] show the according distributions for pions with momentum > 500 MeV. Numbers in brackets in the legend are the integrated multiplicities.

Differential multiplicities w.r.t. kinematic and spacial variables give further insights. The differential multiplicities w.r.t. to the total momentum, the polar angle w.r.t the beam axis in the LAB-frame and the z-position at exit of the target surface are shown in 3, 4 and 5 for π^+ and π^-, respectively, for the reference target. There is a qualitative difference for low- and high-Z materials characterised by a double-peak structure for high-Z materials concerning the total momentum distribution and the fact that low-Z materials tend to give more $\pi^\pm$ with momentum $\gtrsim 600$ MeV than high-Z materials. This is also shown in 5 by the integrated multiplicities when considering only pions with momenta > 500 MeV. Consequently, low-Z materials can provide a wider neutrino energy spectrum due to more high-energetic pions. The angular distribution shows a steep rise with a maximum at about 20° and 30° for low and high-Z materials, respectively, which become shifted to 15° and 20° for pions with momenta > 500 MeV. Moreover, the majority of pions with momenta > 500 MeV is emitted at angles $< 50^\circ$. A qualitative difference between low- and high-Z materials can be seen in 5 in the z-position at target exit which is directly related to twice the nuclear interaction length which is a factor of 2 smaller for high-Z materials. Hence the pions are released already within the first 30 cm of the target whereas for low-Z materials the target might be even chosen longer then 78 cm. This can be seen as an advantage of high-Z materials for pion focusing purposes since they are closer to a point-like source.

	Be	C	Al	AlBeMet	Ta	W	Hg
π^+	0.32	0.33	0.34	0.32	0.23	0.22	0.24
π^-	0.21	0.20	0.21	0.21	0.18	0.17	0.19

Table 5: Total multiplicities of $\pi^\pm$ with momentum > 500 MeV.

The variation of the $E_{\text{kin}}^{\text{bm}}$, L^{tg} and R^{tg} confirms the previous observation, that materials within each group of low- and high-Z materials yield very similar results. This is illustrated in 6 and 7 for both groups for the total multiplicities of $\pi^\pm$ with $E_{\text{kin}}^{\text{bm}} = \{2.2,\, 4.5,\, 8.0\}$ GeV, $L^{\text{tg}} = \{15,\, 30,\, 78\}$ cm and $R^{\text{tg}} = \{7.5,\, 15\}$ mm, but holds also for other particles like γ, n, p^+ and $e^\pm$. In view of the foreseen fixed power of the primary beam rather then fixed number of p.o.t., lower multiplicities at lower $E_{\text{kin}}^{\text{bm}}$ can be compensated by more p.o.t. such that the total number of pions might be comparable to the one at higher energies. This is illustrated by the following example for the Carbon reference target $L^{\text{tg}} = 78$ cm and $R^{\text{tg}} = 15$ mm with the π^+ multiplicities of 0.40, 0.67 and 1.10 for $E_{\text{kin}}^{\text{bm}} = \{2.2,\, 4.5,\, 8.0\}$ GeV, respectively. Once scaling the multiplicities at lower energies with according factors of 8.0/2.2 and 8.0/4.5 in order to account for a fixed power one arrives at 1.45, 1.19 and 1.10 pions per power unit suggesting that lower beam energies indeed yield larger pion numbers. However, the according pion energies are lower too, resulting in a more narrow neutrino energy spectrum. Energies around $E_{\text{kin}}^{\text{bm}} = 4.5$ GeV represent a good compromise providing neutrino spectra with peaks around $(400 - 500)$ MeV and smaller ν_e-backgrounds due to less secondary Kaons compared to $E_{\text{kin}}^{\text{bm}} = 8.0$ GeV where a factor of (3 - 4) more K^+ and K^0 are produced.

A detailed comparison of integrated $\pi^\pm$ multiplicities between C and Hg can be found in 8 for $L^{\text{tg}} = \{7, 15, 30, 78, 90\}$ cm, $R^{\text{tg}} = \{2, 7.5, 15\}$ mm and $E_{\text{kin}}^{\text{bm}} = \{2.2, 4.5, 8.0\}$ GeV. It can be observed, that a saturation is reached once the L^{tg} exceeds twice the nuclear interaction length of the material. Moreover, low-Z materials might profit from a larger radius whereas high-Z materials seem to reabsorb pions if the radius is too large, showing that 7.5 mm might be an optimal value. Low-Z materials yield higher π^+ multiplicities and slightly lower π^- multiplicities than high-Z materials, however, as already shown in the differential multiplicities for the reference target the latter concerns the majority of rather low-energetic π^- with momenta < 500 MeV.

Summarizing, it can be said, that low-Z materials provide

- higher π^+ yield,
- similar π^- yields for momenta > 500 MeV,
- less radiation due to secondary γ, n and $e^\pm$ by a factor of (10 - 20), (10 - 20) and (2 - 3), respectively

than high-Z materials. High-Z materials provide in general higher melting points and the shorter nuclear interaction length enables more localised pion distributions which might be advantageous for focusing with the help of magnetic horns. However, the optimisation of horns in connection with graphite targets yields comparable and even slightly better sensitivities to θ_{13} and δ_{CP} [see section on horn optimisation].

3.3. Target: Energy deposition

The power of the primary beam of several MW leads to huge energy deposition in the target. The interaction of the primary beam is to a large extent determined by the density of the target material and simulations with FLUKA show a factor of $(5 - 6)$ higher energy deposition for high-Z materials compared to low-Z

	Be	C	Al	AlBeMet	Ta	W	Hg
E/pulse [kJ/pulse]	3.39	4.03	5.73	4.09	23.6	25.4	20.7
power [kW]	169.5	201.5	286.6	204.8	1180	1272	1036

Table 6: Deposited energy/pulse and power in reference target for primary beam parameters $E_{\rm kin}^{\rm bm} = 4.5$ GeV, $\sigma^{\rm bm} = 0.0$ mm at 50 Hz and 4 MW.

materials. 6 summarises the results for the reference target with primary beam $E_{\rm kin}^{\rm bm} = 4.5$ GeV, point-like beam spot ($\sigma^{\rm bm} = 0.0$ mm) and at a frequency of 50 Hz (energy/pulse) and power of 4 MW (assuming a continuous beam). When using more realistic beam profiles width a gaussian width in x- and y-direction of 4 mm (8 mm) the deposited power drops down to 97 % (75 %) due to the inifinite size of the beam spot. 9 shows the power density in the reference target for C and Ta for beam widths $\sigma^{\rm bm} = 0.0$ mm and $\sigma^{\rm bm} = 0.4$ mm in the z-y plane at $x \in [-0.05, +0.05]$ cm. The maximal values of the power density are about one order higher in high-Z materials compared to low-Z ones, located in the first nuclear interaction length of the target.

material	$\sigma^{\rm bm}$ [mm]	max power density [kW/cm^3]	total power [kW]	with magn. field (+I, -I)
Be	2	11.65	168.7	(+6 %, +4 %)
	4	3.25	165.3	(+6 %, +4 %)
	6	1.53	153.2	(+12 %, +4 %)
C	2	13.22	200.0	(+6 %, +5 %)
	4	3.57	196.5	(+7 %, +4 %)
	6	1.72	182.2	(+12 %, +4 %)
AlBeMet	2	14.11	204.4	(+7 %, +5 %)
	4	3.92	200.1	(+7 %, +5 %)
	6	1.86	185.2	(+13 %, +5 %)
Al	2	19.26	285.6	(+8 %, +6 %)
	4	5.36	279.1	(+8 %, +6 %)
	6	2.73	257.4	(+14 %, +6 %)

Table 7: The maximal value of deposited power density assuming a continuous proton beam and the total power deposited in the target at various values of the beam width $\sigma^{\rm bm}$. The last column indicates the increase of the total power in the presence of the magnetic field of the horn directly at target surface, see text for more details.

Besides the total energy deposited it is desirable to distribute the energy within the target as homogeneously as possible in order to reach rather low values of the energy density. This can be achieved with an appropriate beam profile and accordingly optimal size of the beam spot compared to the target cross section. The longer interaction nuclear interaction length of low-Z materials turns out to be advantageous in this respect [see 9]. The maximal values of the deposited power density in low-Z materials are shown in 7 for a gaussian beam profile with beam width $\sigma^{\mathrm{bm}} = \{2,\, 4,\, 6\}$ mm assuming a continuous beam of 4 MW. The pulsed temporal beam structure with pulse duration of about 1 μs leads in reality to much higher power depositions during the pulse (or bunch within a pulse) with gaps of about 20 ms or 80 ms depending on the repetition frequency of 50 Hz or 12.5 Hz of the primary beam for the setups of 1- and 4-target-horn stations, respectively. Needless to say, that the deposited power is reduced by a factor of 4 for the setup of 4-target-horn stations in parallel.

In the case that the target is an integral part of the inner horn conductor, the magnetic field of the horn will act on charged particles immediately when exiting the target surface[2] and increase in general the energy deposition due to redirecting particles with low transverse momenta into the target. The additional increase in power deposition is given in the last column of 7 for positive $(+I)$ and negative $(-I)$ charged particle focusing mode of the horn and results in a slight increase of (4 - 8) %. Here a horn current of $I = \pm 300$ kA has been assumed which generates a magnetic field strength of about $B = 4$ Tesla at $R^{\mathrm{tg}} = 15$ mm. The strong rise in positive focusing mode at large beam width $\sigma^{\mathrm{bm}} = 6$ mm is caused by the infinite size of the beam spot due to the protons which arrive at radii $> R^{\mathrm{tg}}$. They are absent in a realistic setup due to the finite beam spot, provided it is kept smaller than the target radius.

9 shows the distribution of the deposited power in the C-target for different values of $\sigma^{\mathrm{bm}} = \{0.0,\, 0.4\}$ mm. The results for Be, Al and AlBeMet are qualitatively similar as can be seen in projections on z and r in 10 and 11, respectively, for a beam width of $\sigma^{\mathrm{bm}} = 4$ mm. 10 shows the power density depending on z for the central bin $r \in [0, 0.5]$ mm. In the C-target (Al-target) it is around a value of 3.5 kW/cm^3 (5 kW/cm^3) within the first 5 cm of the target and then it drops down to 0.4 kW/cm^3 (0.3 kW/cm^3) at $z = 78$ cm. 11 shows the radial dependence of the power density at different values of $z \in$

[2]A possible magnetic field inside the target due to the horn current has been neglected in the simulation.

$[0.5, 1.0]$, $[10, 10.5]$, $[30, 30.5]$, $[60.0, 60.5]$ cm. In general the energy deposition is lowest in Be, followed by C and AlBeMet. The higher density of Al leads to the largest energy depositions.

3.4. Target cooling -Chris-Benjamin

3.5. Thermomechanical Analysis Chris-Benjamin

4. The horn-Marcos

4.1. Horn conceptual design-Marcos

4.2. The energy deposition-Andrea

4.3. Horn cooling-Piotr

4.4. Horn Thermomechanical Analysis-Piotr

5. The horn and target integration-Piotr

5.1. Horn and target integration drawings-Piotr-Valeria

6. Conclusions

Acknowledgments

We acknowledge the financial support of the European Community under the European Commission Framework Programme 7 Design Study: EUROnu, Project Number 212372. The EC is not liable for any use that may be made of the information contained herein.

References

[1] C. Bobeth, O. Caretta, P. Cupial, T. Davenne, C. Densham, M. Dracos, M. Fitton, M. Kozien, A. Longhin, P. Loveridge, F. Osswald, M. Rooney, B. Skoczen, A. Wroblewski and M. Zito, "The proton driver for the neutrino Super Beam: status and issues," EUROnu WP2 Note 09-11, http://www.euronu.org/.

[2] G. Battistoni, S. Muraro, P. R. Sala, F. Cerutti, A. Ferrari, S. Roesler, A. Fassò and J. Ranft, "The FLUKA code: Description and benchmarking," AIP Conf. Proc. **896**, 31 (2007);
A. Ferrari, P. R. Sala, A. Fassò and J. Ranft, "FLUKA: A multi-particle transport code (Program version 2005)," CERN-2005-010, SLAC-R-773, INFN-TC-05-11.

[3] S. E. Kopp, "Accelerator neutrino beams," Phys. Rept. **439**, 101 (2007) [arXiv:physics/0609129].

[4] S. van der Meer, "A directive device for charged particles and its use in an enhanced neutrino beam," CERN-61-07.

[5] M. Baylac *et al.*, “Conceptual design of the SPL II : A high-power superconducting H^- linac at CERN,” CERN-2006-006;
O. Brunner *et al.*, “Assessment of the basic parameters of the CERN SPL,” CERN-AB-2008-067 BI/RF.

[6] A. de Bellefon *et al.*, “MEMPHYS: A large scale water Cerenkov detector at Frejus,” arXiv:hep-ex/0607026.

[7] A. E. Ball, A. Blondel, S. S. Gilardoni and N. Vassilopoulos, “Preliminary magnetic horn studies in the collection scheme for a neutrino factory,” Nucl. Instrum. Meth. A **451**, 359 (2000).
A. E. Ball, N. Vassilopoulos, A. Blondel and S. S. Gilardoni, “Updated results of the horn study for the Nufact,” Nucl. Instrum. Meth. A **472**, 650 (2000), CERN-NUFACT-NOTE-42, CERN-OPEN-2000-339.

[8] S. S. Gilardoni, “Study of particle production and capture for a neutrino factory,” CERN-THESIS-2004-046, CERN-NUFACT-NOTE-141, GENEVA-THESE-3536, Jul 2004.

[9] S. S. Gilardoni, G. Grawer, G. Maire, J. M. Maugain, S. Rangod and F. Voelker, “Status of a magnetic horn for a neutrino factory,” J. Phys. G **29**, 1801 (2003).

[10] J. E. Campagne and A. Cazes, “The theta(13) and delta(CP) sensitivities of the SPL-Frejus project revisited,” Eur. Phys. J. C **45**, 643 (2006) [arXiv:hep-ex/0411062].

[11] J. E. Campagne, “Horn profile determination: The SPL use case,” CERN-NUFACT-NOTE-138, Jul 2004.

[12] J. E. Campagne, M. Maltoni, M. Mezzetto and T. Schwetz, “Physics potential of the CERN-MEMPHYS neutrino oscillation project,” JHEP **0704**, 003 (2007) [arXiv:hep-ph/0603172].

[13] C. Bobeth, G. Gaudiot and B. Lepers, “Water cooled solid target for high power neutrino SPL-Super Beam,” EUROnu-WP2-Note 10-XY.

[14] T. Nakadaira *et al.*, “T2K target,” AIP Conf. Proc. **981**, 290 (2008).

[15] A. Longhin, “Study of the performance of the SPL-Fréjus Super Beam using a graphite target,” EUROnu WP2 Note 09-01, http://www.euronu.org/.

[16] A. Blondel, S. S. Gilardoni and M. Donega, "Neutrino fluxes from a conventional neutrino beam using CERN SPL," CERN-NUFACT-NOTE-53, CERN-OPEN-2000-343, Nov 2000;
A. Blondel, M. Donega and S. S. Gilardoni, "Study of (anti-)neutrino fluxes from a horn neutrino beam using 2.2-GeV protons," CERN-NUFACT-NOTE-078, CERN-NUFACT-NOTE-78, Sep 2001.

[17] A. Cazes, "Study of the CNGS beam and muon identification with the OPERA experiment. Optimization of the SPL-Frejus project beam line," LAL-04-118, Ph.D. Thesis, Dec 2004.

[18] P. Huber, M. Lindner and W. Winter, Comput. Phys. Commun. **167**, 195 (2005) [arXiv:hep-ph/0407333];
P. Huber, J. Kopp, M. Lindner, M. Rolinec and W. Winter, Comput. Phys. Commun. **177**, 432 (2007) [arXiv:hep-ph/0701187].

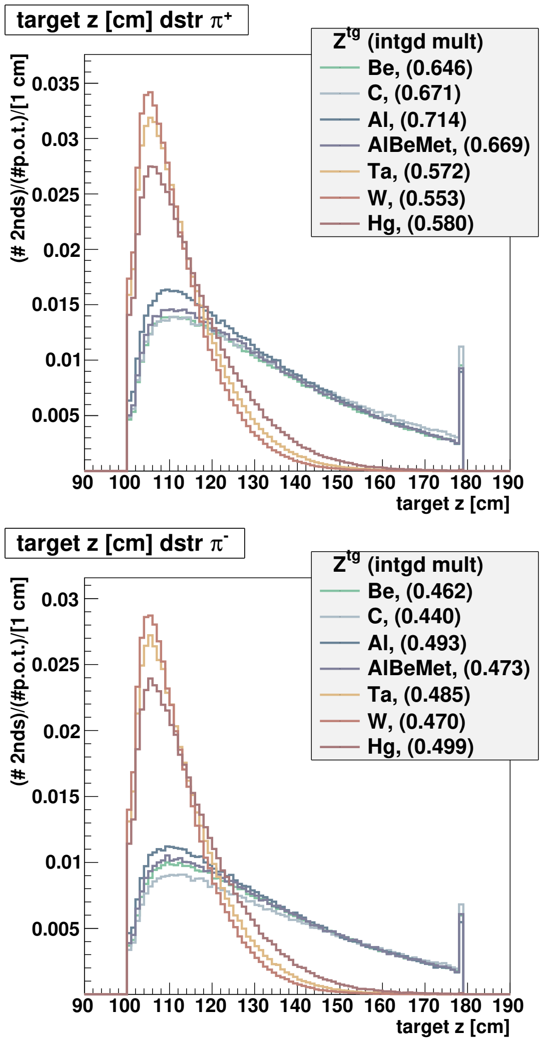

Figure 5: The differential multiplicity distribution of π^+ [left] and π^- [right] w.r.t. the z position at exit of the target surface (note an off-set of $+100$ cm) for the reference target for low atomic number materials Be, C, Al and compound AlBeMet compared with high atomic number materials Ta, W and Hg. Numbers in brackets in the legend are the integrated multiplicities.

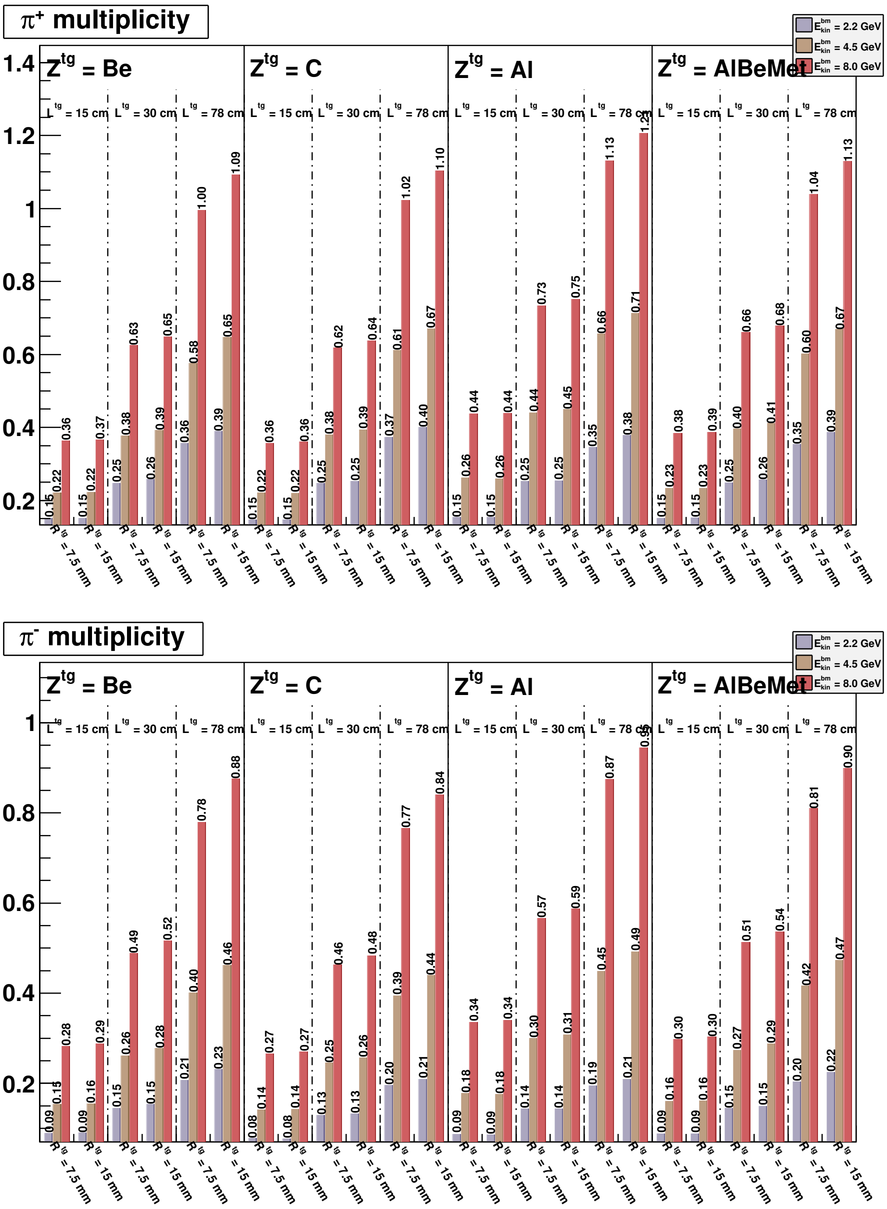

Figure 6: The multiplicity of π^+ [upper] and π^- [lower] for low-Z materials varying $L^{\rm tg}$ = $\{15,\, 30,\, 78\}$ cm, $R^{\rm tg} = \{7.5,\, 15\}$ mm and $E^{\rm bm}_{\rm kin} = \{2.2,\, 4.5,\, 8.0\}$ GeV.

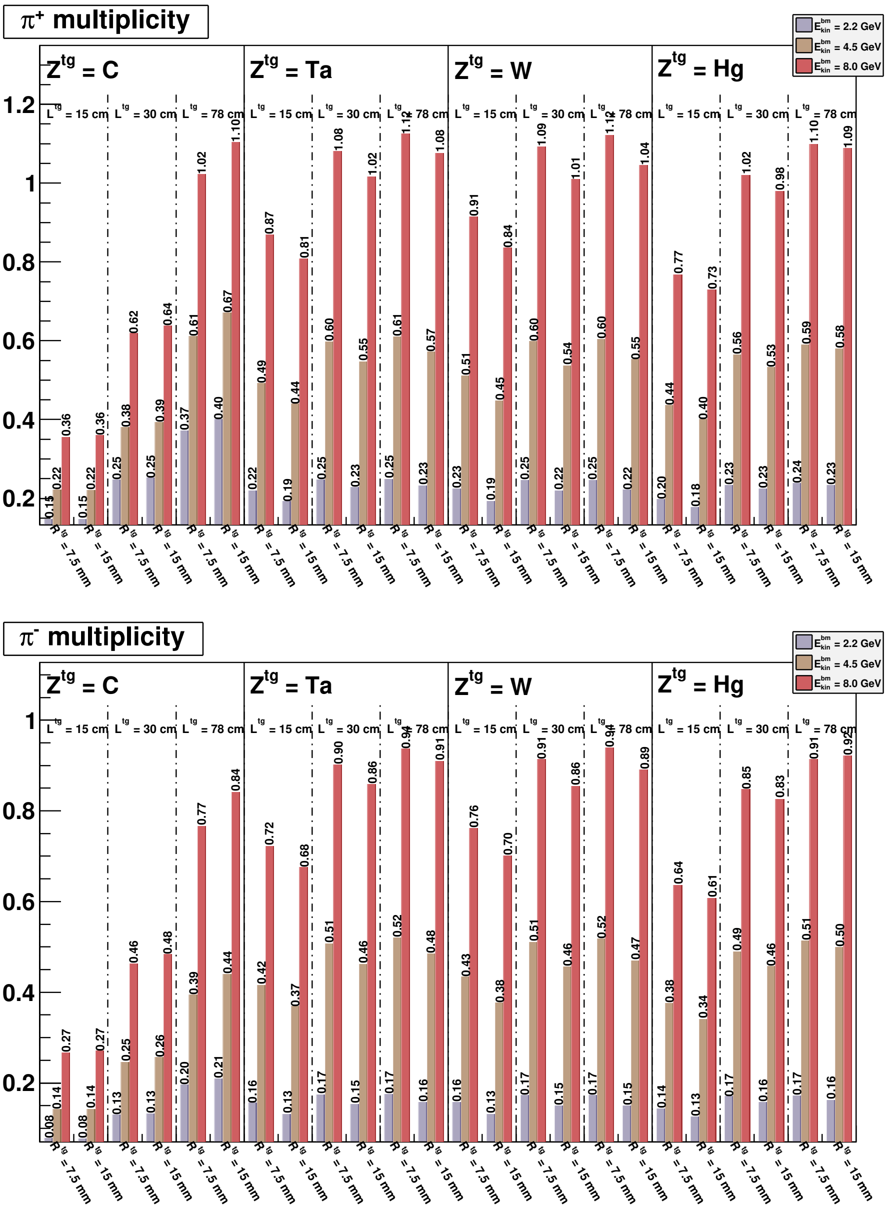

Figure 7: The multiplicity of π^+ [upper] and π^- [lower] for high-Z materials (and C for comparison) varying $L^{\rm tg} = \{15,\ 30,\ 78\}$ cm, $R^{\rm tg} = \{7.5,\ 15\}$ mm and $E^{\rm bm}_{\rm kin} = \{2.2,\ 4.5,\ 8.0\}$ GeV.

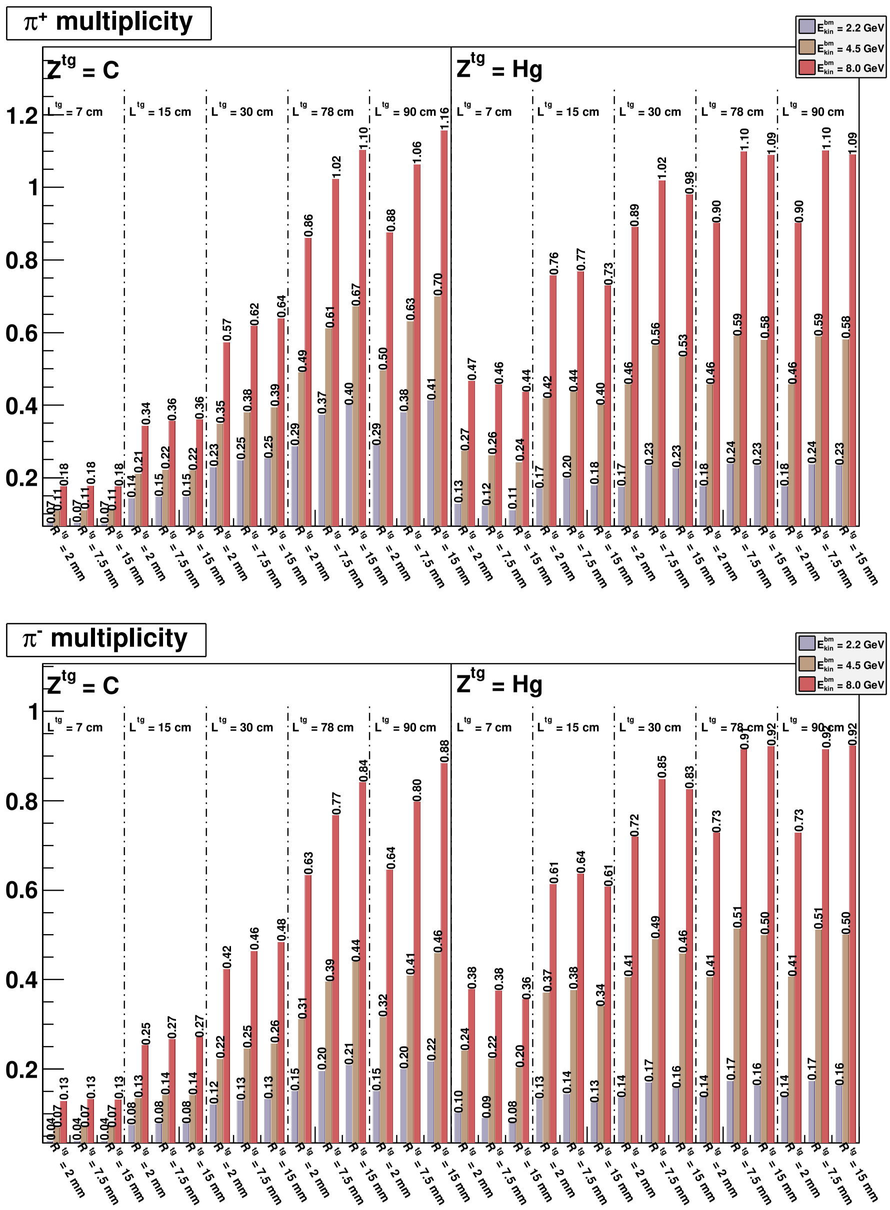

Figure 8: The multiplicity of π^+ [upper] and π^- [lower] for C and Hg materials varying $L^{\rm tg} = \{7,\,15,\,30,\,78,\,90\}$ cm, $R^{\rm tg} = \{2,\,7.5,\,15\}$ mm and $E^{\rm bm}_{\rm kin} = \{2.2,\,4.5,\,8.0\}$ GeV.

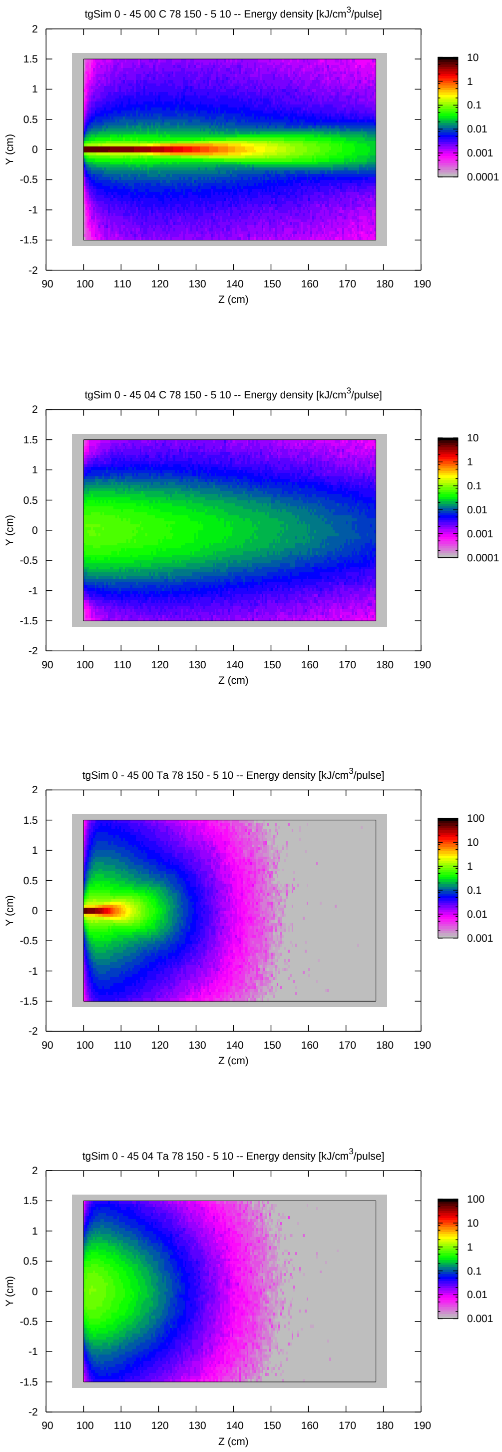

Figure 9: The power deposition in the z-y plane at $x \in [-0.05, +0.05]$ cm in the reference target for C [upper] and Ta [lower] for beam width $\sigma^{\rm bm} = 0.0$ mm [left] and $\sigma^{\rm bm} = 0.4$ mm [right].

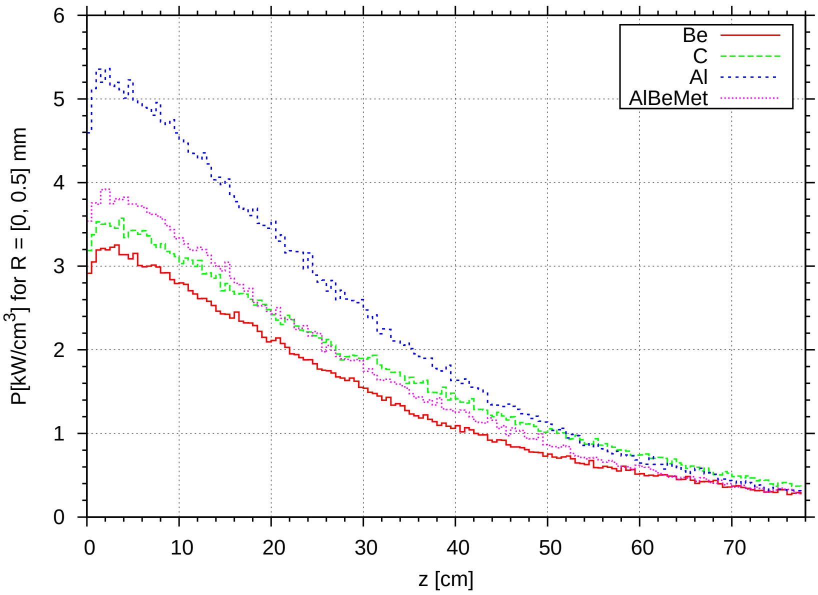

Figure 10: Distribution of deposited power in [kW/cm^3] from the beam w.r.t. z at $r \in [0, 0.5]$ mm in the targets for $P^{\rm bm} = 4$ MW and $\sigma^{\rm bm} = 4$ mm.

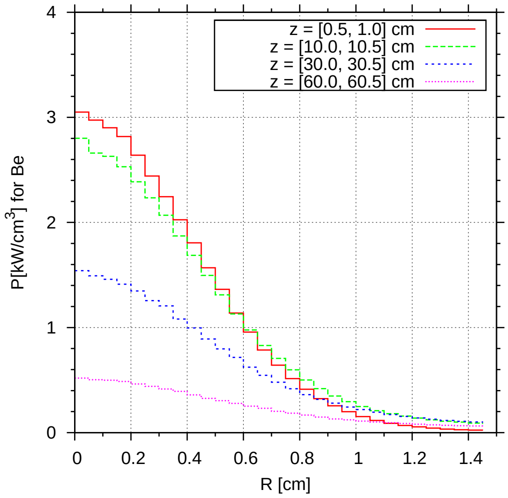

a) Be-target

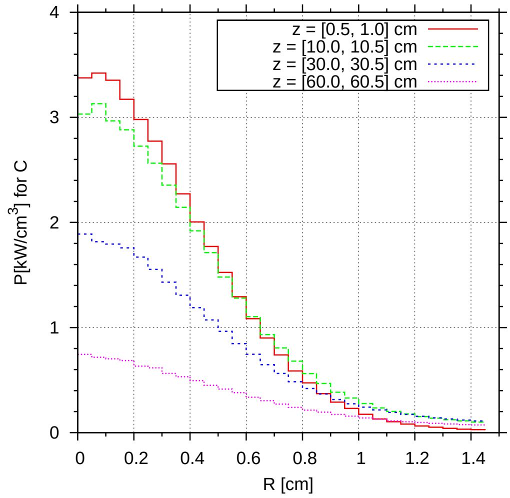

b) C-target

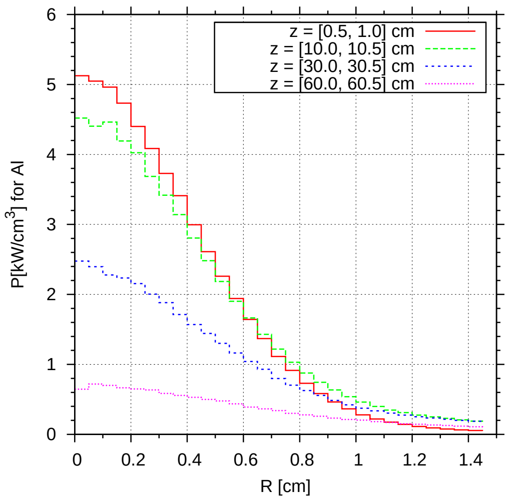

c) Al-target

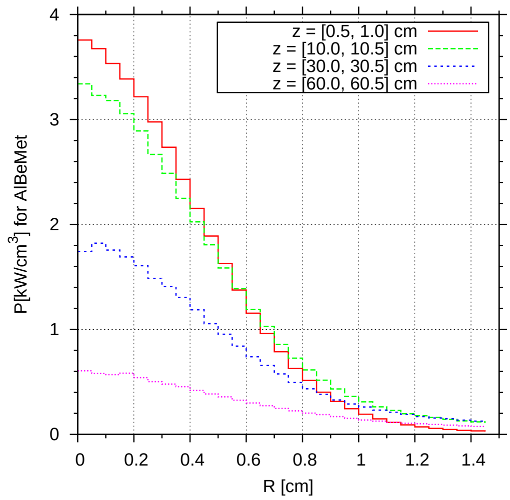

d) AlBeMet-target

Figure 11: Distribution of deposited power for the targets in [kW/cm^3] from the beam w.r.t. r at different z for $P^{\mathrm{bm}} = 4$ MW and $\sigma^{\mathrm{bm}} = 4$ mm.